

Contents lists available at ScienceDirect

Petroleum Science

journal homepage: www.keaipublishing.com/en/journals/petroleum-science



Original Paper

Stability of high-salinity-enhanced foam: Surface behavior and thinfilm drainage



Lin Sun a , Xue-Hui Sun a , Yong-Chang Zhang b , Jun Xin c , Hong-Ying Sun a , Yi-Bo Li a , Wan-Fen Pu a , Jin-Yu Tang d , Bing Wei a , **

- ^a National Key Laboratory of Oil and Gas Reservoir Geology and Exploitation, Southwest Petroleum University, Chengdu, 610500, Sichuan, China
- ^b No. 9 Oil Production Plant, PetroChina Changqing Oilfield Company, Yinchuan, 750006, Gansu, China
- c Research Institute of Geological Exploration and Development, CNPC Chuanqing Drilling Engineering Company Limited, Chengdu, 610501, Sichuan, China
- ^d Department of Chemical and Petroleum Engineering, United Arab Emirates University, Al Ain, Abu Dhabi, 15551, United Arab Emirates

ARTICLE INFO

Article history: Received 30 May 2022 Received in revised form 12 January 2023 Accepted 14 January 2023 Available online 16 January 2023

Edited by Yan-Hua Sun

Keywords:
High-salinity reservoirs
Betaine foam
Foam stability
Dilatational viscoelasticity
Disjoining pressure
Thin-film interferometry

ABSTRACT

Cocamidopropyl hydroxyl sulfobetaine (CHSB) is one of the most promising foaming agents for high-salinity reservoirs because the salt in place facilitates its foam stability, even with salinity as high as 2×10^5 mg/L. However, the synergistic effects between CHSB and salt have not been fully understood. This study utilized bulk foam tests and thin-film interferometry to comprehensively investigate the macroscopic and microscopic decay processes of CHSB foams with NaCl concentrations ranging from 2.3×10^4 to 2.1×10^5 mg/L. We focused on the dilatational viscoelasticity and dynamic thin-film thickness to elucidate the high-salinity-enhanced foam stability. The increase in dilatational viscoelasticity and supramolecular oscillating structural force (Π_{OS}) with salinity dominated the superior stability of CHSB foam. With increasing salinity, more CHSB molecules accumulated on the surface with a lower diffusion rate, leading to high dilatational moduli and surface elasticity, thus decelerating coarsening and coalescence. Meanwhile, the number density of micelles in the thin film increased with salinity, resulting in increased Π_{OS} . Consequently, the energy barrier for stepwise thinning intensified, and the thin-film drainage slowed. This work conduces to understand the mechanisms behind the pronounced stability of betaine foam and can promote the widespread application of foam in harsh reservoirs.

© 2023 The Authors. Publishing services by Elsevier B.V. on behalf of KeAi Communications Co. Ltd. This is an open access article under the CC BY-NC-ND license (http://creativecommons.org/licenses/by-nc-nd/

4.0/).

1. Introduction

Enhanced oil recovery is the top priority to secure the oil supply. Enhanced oil recovery methods, including gas injection, chemical flooding, and steam injection, have been proven viable and profitable in academia and industry (Ghosh and Mohanty, 2019; Xun, 2021; Khan et al., 2021; Tang and Sheng, 2022; Agra and Tayfun, 2022). However, the inherent drawbacks, such as channeling and gravity override, severely limit their performance. Therefore, foam is employed to control mobility and conformance, the efficiency of which is directly determined by foam stability (Hu et al., 2020; Roncoroni et al., 2021; Liu Q. et al., 2022). However, because foam is a thermodynamic instability system, maintaining its stability is

E-mail addresses: slswpu@swpu.edu.cn (L. Sun), bwei@swpu.edu.cn (B. Wei).

difficult, especially in high-temperature, high-salinity reservoirs (Suja et al., 2018; Syed et al., 2020; Li et al., 2020; Yang et al., 2021; Said et al., 2022). Liu Z.M. et al. (2022) have reported that foamability and foam stability of sodium dodecyl diphenyl ether disulfonate and sodium alpha-olefin sulfonate (AOS) are very poor at the salinity of 2.5 \times 10^5 mg/L. Kang et al. (2021) have found that the foam stability of sodium fatty alcohol polyoxyethylene ether carboxylates/SiO2 gradually weakens with increasing salinity, even with the maximum salinity $<\!6\times10^4$ mg/L.

Recently, there has been an increasing interest in applying betaine foam in high-temperature, high-salinity environments owing to its excellent tolerance to such temperatures and salinity (Hongyan et al., 2017; Alzobaidi et al., 2017; Da et al., 2018; Sun et al., 2019). Moreover, researchers have reported that betaine surfactants, for example, cocamidopropyl hydroxyl sulfobetaine (CHSB), had synergistic effects with salt and could generate high-salinity-enhanced foam, the stability of which increased with salinity (up to 2×10^5 mg/L) (Sun et al., 2016; Varade and Ghosh,

^{*} Corresponding author.

^{**} Corresponding author.

2017; Da et al., 2018; Li et al., 2019). Despite betaine foam holding the potential for improving oil production in high-salinity reservoirs, little attention has been paid to the mechanisms behind its superior foam stability, mainly because of the complexity of the foam decay process and the lack of visual tools to characterize the evolution of the thin film. This severely limits the development of foam technology in harsh reservoirs.

Bulk foam usually undergoes three processes: drainage, coarsening (Ostwald ripening), and coalescence (Fig. 1) (Kedir et al., 2022). Drainage is driven by gravity and capillary pressure, coarsening originates from the pressure difference between the different size bubbles, and the rupture of the film between adjacent bubbles triggers coalescence. The factor that changes the velocity of any of these three processes will affect the foam stability, for example, liquid viscosity, gas diffusivity, and polydispersity of bubble sizes. The film thickness influences the velocity of all three processes, and the thicker the liquid film, the slower the decay of bulk foam. However, the film thickness decreases with drainage. The high surface viscoelasticity can decrease surface mobility and restrain the stretch of the film, thus decelerating the drainage of thick films and coarsening (Tcholakova et al., 2011; Keshavarzi et al., 2020; Shi et al., 2022). When the film thickness approaches ~100 nm, the disjoining pressure (Π) governs the film thickness and hence the foam stability (Radke, 2015; Zhang and Sharma, 2018; Babamahmoudi and Riahi, 2018; Langevin, 2020).

The disjoining pressure consists primarily of DLVO forces, including van der Waals attraction and electrostatic double-laver repulsion, for micelle-free thin films formed by ionic surfactants (Ninham et al., 2017). As shown in Fig. 2a, the magnitude of the disjoining pressure is strongly dependent on the film thickness, and a common black film presents when the disjoining pressure counterbalances the capillary pressure (P_c) . The shorter ranged non-DLVO forces, that is, the solvation force (generated by hydration and hydrophobicity) and steric force, operate when the film thickness is about a few nanometers. Subsequently, the Newton black film presents (Langevin, 2020). However, for micellar thin films, the disjoining pressure additionally comprises a longer ranged non-DLVO force because of the micellar layering, called a supramolecular oscillatory structural force (Π_{OS}) (Lee et al., 2017). The oscillation properties of Π_{OS} cause the successive equilibrium of the disjoining pressure and the capillary pressure. Therefore, multiple metastable thicknesses, such as h_a and h_b in Fig. 2b, appear during thin-film drainage.

Foam stability highly depends on the surface viscoelasticity and disjoining pressure, so they are combined to elucidate the high-salinity enhanced stabilization of CHSB foam. We performed systematic bulk foam tests and thin-film interferometry measurements to probe the effect of salinity on foam decay from both macroscopic and microscopic perspectives. Comprehensive surface behavior analyses, including dilatational viscoelasticity, absorption capability, and diffusion rate, were conducted to clarify their

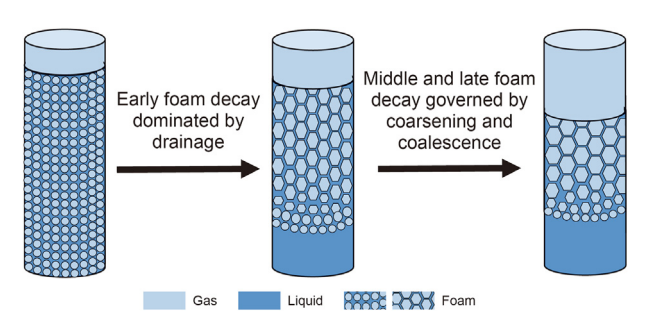


Fig. 1. The decay process of bulk foam.

relationship with foam stability. The colorimetric method and supramolecular oscillating structural force were merged to investigate the spatial-temporal evolution of thin-film thickness. The obtained results will advance and deepen the present knowledge of betaine foam, which is helpful for the development of foamenhanced oil recovery methods.

2. Materials and methods

2.1. Materials

CHSB with a mass concentration of 35 wt% was purchased from Yusuo Chemical Technology Co., Ltd. Its chemical molecular structure is given in Fig. 3. Brine $(2.3 \times 10^4 - 2.1 \times 10^5 \text{ mg/L NaCl solution})$ was prepared by dissolving sodium chloride (NaCl) in deionized water.

2.2. Foamability and foam stability assessment

Foam was generated through the Waring blender method. First, the CHSB solution and a graduated cylinder were preheated to 90 °C. Then, 100 mL of CHSB solution was stirred in a Waring blender for 1 min at 6000 rpm. The generated foam was immediately transferred into the graduated cylinder to measure the initial foam volume. The graduated cylinder was sealed and placed in a visualization thermostat (at 90 °C) to record the variations of foam volume (V_f) and drained liquid volume (V_l) over time. The foam half-life when 50 mL of liquid drained from the foam was used to estimate the foam stability. The liquid volume fraction (f_w) is defined as follows:

$$f_{\rm W} = \frac{100 - V_{\rm l}}{V_{\rm f}} \times 100\% \tag{1}$$

2.3. Surface behavior measurements

The DSA100 Drop Shape Analyzer (DDSA) was utilized to assess the surface behavior of the CHSB solution at 20 $^{\circ}$ C.

2.3.1. Dilatational rheology tests

Dilatational rheology is typically characterized by the dilatational modulus (E), which is composed of the elastic modulus (E') and viscous modulus (E") (Amani et al., 2020).

$$E = E' + iE'' \tag{2}$$

The dilatational modulus *E* can be estimated from

$$E = \frac{\mathrm{d}\gamma}{\mathrm{dln}A} \tag{3}$$

where γ is the surface tension; A is the surface area. The oscillation drop method was used to obtain the dilatational rheology. In a typical test, a CHSB droplet of 10 μ L was extruded from an injector through a syringe pump installed on the DDSA. Periodic oscillations at a fixed amplitude of 10% were imposed on the droplet after attaining the equilibrium state of surface tension. The oscillation frequency was 0.02–2 Hz, and the values of E, E', and E'' were automatically calculated by the DDSA.

2.3.2. Surface tension tests

The surface tension was measured using the pendant drop method. A CHSB droplet was generated at the needle end of an injector in the same way as in the dilatational rheology test. The

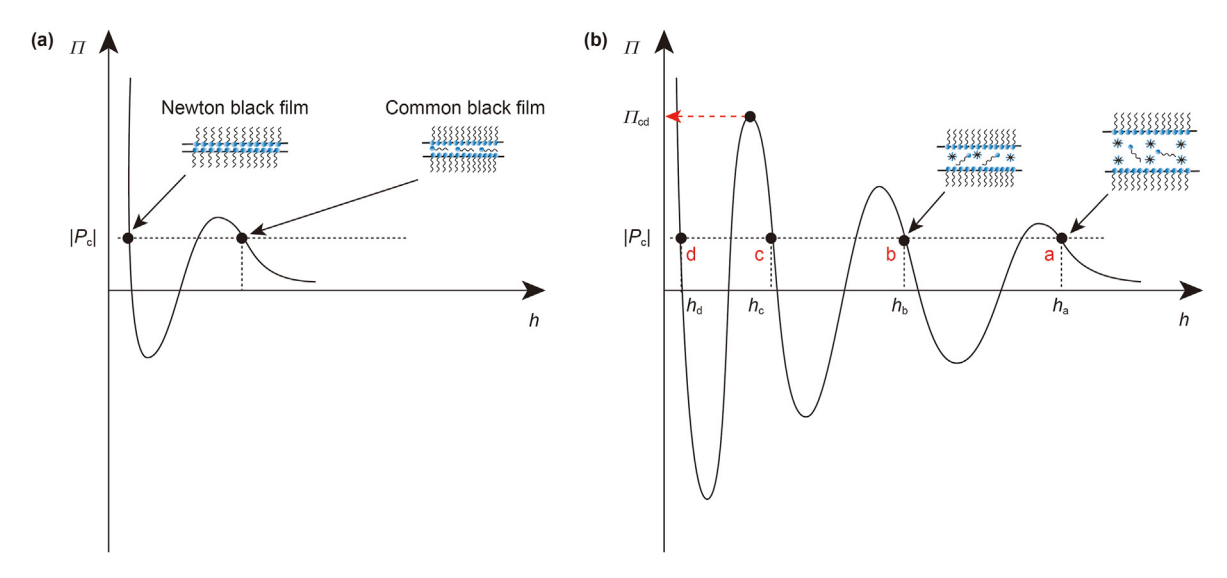


Fig. 2. Disjoning pressure (Π) curves for the thin films (**a**) without micelles (surfactant concentration c < CMC) and (**b**) with micelles (c > CMC).

Fig. 3. Molecular structure of CHSB.

droplet shape was recorded with time by the DDSA to calculate the dynamic surface tension and equilibrium surface tension (γ_{eq}).

The $\gamma_{\rm eq}$ as a function of CHSB concentration was measured. The maximum surface excess concentration ($\Gamma_{\rm max}$) and the minimum area occupied by each molecule ($A_{\rm min}$) were determined using (Niu et al., 2017; Xie et al., 2018).

$$\Gamma_{\text{max}} = -\frac{1}{2.303nRT} \left(\frac{\text{d}\gamma}{\text{dlog}c} \right) \tag{4}$$

$$A_{\min} = \frac{1}{N_{\rm A} \Gamma_{\max}} \tag{5}$$

where c is the surfactant concentration; $d\gamma/d\log c$ is the slope of the curve below the CMC; R is the universal gas constant; T is the absolute temperature; n is related to the type of surfactant (in the test, n=1); and N_A is Avogadro's number.

2.4. Dynamic drainage of thin film

Thin-film interferometry and the colorimetric method were combined to quantitatively characterize the spatial and temporal evolution of the thin film.

2.4.1. Thin-film interferogram

The experimental setup shown in Fig. 4 was used to visualize the thin-film drainage non-invasively and capture the interferograms. The basic principle of this experiment was similar to the interferometry digital imaging optical microscopy method (Zhang and Sharma, 2015). The CHSB solution was injected into the cylindrical Scheludko-like cell in the glass slide with a syringe. A plane-parallel thin film and a thicker meniscus region were generated,

functioning as the parallel film and plateau border in a foam, respectively. The thin film was illuminated vertically by the white light of the metallographic microscope (DM2700M, Leica Ltd., Germany), which was set at a reflected light mode. Interference occurred between the light rays reflected from the two planeparallel surfaces of the thin film, and the interferograms during the thin-film drainage were recorded by the data acquisition system.

2.4.2. Thin-film thickness

The color in the interferogram of a thin film was determined by the film thickness. With the help of the interference color chart, the decay of film thickness could be obtained based on the captured interferograms during thin-film drainage.

2.4.2.1. Interference color chart. Each pixel in the interferogram corresponded to unique *X*, *Y*, and *Z* tristimulus values and *R*, *G*, and *B* values. The *X*, *Y*, and *Z* tristimulus values were calculated using the following equations (Eiki et al., 2003; Liu et al., 2010):

$$X = K \int_{380}^{780} S(\lambda)\overline{x}(\lambda)R(\lambda)d\lambda \cong K \sum_{380}^{780} S(\lambda)\overline{x}(\lambda)R(\lambda)$$

$$Y = K \int_{380}^{780} S(\lambda)\overline{y}(\lambda)R(\lambda)d\lambda \cong K \sum_{380}^{780} S(\lambda)\overline{y}(\lambda)R(\lambda)$$

$$Z = K \int_{380}^{780} S(\lambda)\overline{z}(\lambda)R(\lambda)d\lambda \cong K \sum_{380}^{780} S(\lambda)\overline{z}(\lambda)R(\lambda)$$

$$K = 100 / \int_{380}^{780} S(\lambda)\overline{y}(\lambda)d\lambda = 100 / \sum_{380}^{780} S(\lambda)\overline{y}(\lambda)$$
(6)

where $S(\lambda)$ is the spectrum power of white light at a certain light wavelength (λ) ; $\overline{x}(\lambda)$, $\overline{y}(\lambda)$, and $\overline{z}(\lambda)$ are the color matching function of the XYZ standard colorimetric system of CIE 1931, respectively; and $R(\lambda)$ is the energy light reflectance at λ . The distributions of $S(\lambda)$, $\overline{x}(\lambda)$, $\overline{y}(\lambda)$, and $\overline{z}(\lambda)$ are shown in Fig. 5. When the incident light was perpendicular to the thin film, $R(\lambda)$ was calculated as follows.

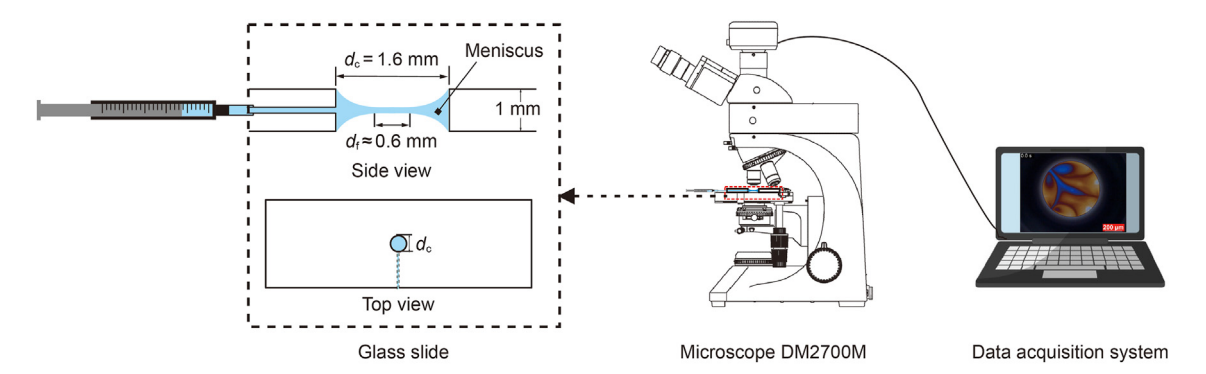


Fig. 4. Schematic of the experimental setup for visualizing the drainage of thin films.

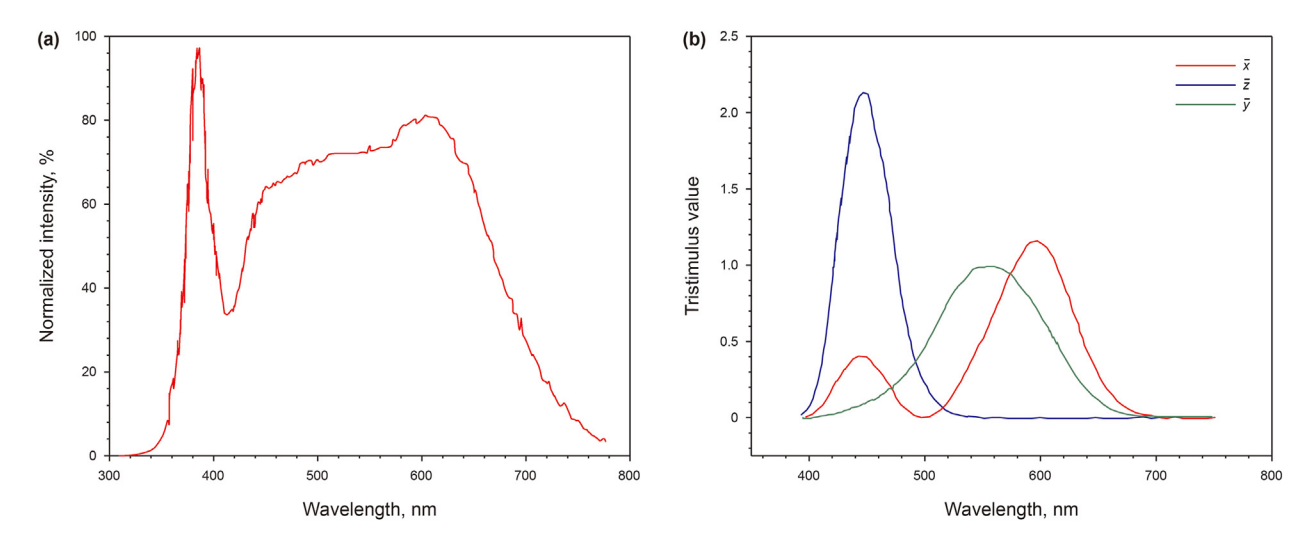


Fig. 5. (a) Spectrum power distribution of white light. (b) Color matching function of the XYZ standard colorimetric system of CIE 1931.

$$R(\lambda) = 1 - \frac{8n_0n_1^2n_2}{\left(n_0^2 + n_1^2\right)\left(n_1^2 + n_2^2\right) + 4n_0n_1^2n_2 + \left(n_0^2 - n_1^2\right)\left(n_1^2 - n_2^2\right)\cos(4\pi n_1 h/\lambda)}$$
 (7)

where n_0 and n_2 are the refractive indices of air $(n_0 = n_2 = 1)$; n_1 is the refractive index of the thin liquid film $(n_1 = 1.33)$; and h is the film thickness.

The *R*, *G*, and *B* values were transformed from the *X*, *Y*, and *Z* tristimulus values according to

$$\begin{bmatrix} r \\ g \\ b \end{bmatrix} = \begin{bmatrix} 3.5064 & -1.7400 & -0.5441 \\ -1.0690 & 1.9777 & 0.0352 \\ 0.0563 & -0.1970 & 1.05711 \end{bmatrix} \times \begin{bmatrix} X \\ Y \\ Z \end{bmatrix}$$
(8)

$$R = \frac{r}{M} \times 255$$
, $G = \frac{g}{M} \times 255$, $B = \frac{b}{M} \times 255$ (9)

where r, g, and b are the chromaticity coordinates; and M is the maximum among the r, g, and b values.

According to Eqs. (6)—(9), the R, G, and B values corresponding to the film thickness of 0 and 250 nm were calculated and converted into the interference color, as presented in Fig. 6.

2.4.2.2. Film thickness. A square region with a side of 25 μ m located in the center of the interferogram was selected as a study point and converted into pixels, each of which was split into R, G, and B values using the Color Split Channels module of the commercial software ImageJ. Afterward, all the R, G, and B values were averaged to R_i , G_i , and B_i , respectively. The following equation was used to determine the pixel point in the color chart that minimized d_E , called the reference point:

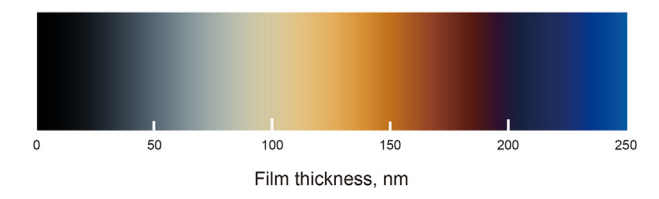


Fig. 6. Synthesized interference color chart of white light. From 0 to 250 nm film thickness, the color sequentially forms black, gray, orange, and blue.

$$d_{\rm E} = \sqrt{(R_i - R_j)^2 + (G_i - G_j)^2 + (B_i - B_j)^2}$$
 (10)

where R_j , G_j , and B_j values are the R, G, and B values of a random pixel point in the color chart. The film thickness of the study point was equal to that of the reference point.

2.4.2.3. Three-dimensional (3D) thickness map reconstruction. First, the pixel points in the whole interferogram were split into *R*, *G*, and *B* values through Image J. Then, the film thickness of each pixel point was calculated using Eq. (10). Finally, the 3D Surface Plot module of Image J was utilized to reconstruct the 3D map of the film thickness.

3. Results and discussion

3.1. Response of foam stability to salinity

The volume and half-life of CHSB foam were measured at a series of NaCl concentrations ($2.3 \times 10^4 - 2.1 \times 10^5$ mg/L) to estimate the effect of salinity on its foamability and foam stability. A wide CHSB concentration range of 0.05 wt% to 1.00 wt% was used in this experiment.

Fig. 7a illustrates that foamability increases with CHSB concentration and its response to salinity is affected by CHSB concentration. As salinity increased, the foam volume was almost unchanged when the CHSB concentration was 0.05 wt%, whereas it decreased when the CHSB concentration was > 0.20 wt%. However, the foam volume decreased by < 38% even though the NaCl concentration increased from 2.3 \times 10⁴ to 2.1 \times 10⁵ mg/L. The effects of salinity and CHSB concentration on foam stability differed significantly from those on foamability. Fig. 7b reveals that the foam halflife increases with salinity throughout the tested CHSB concentrations. For example, the foam half-life at 2.1×10^5 mg/L NaCl was a factor of 6.5 longer than that at 2.3×10^4 mg/L NaCl when the CHSB concentration was 0.05 wt%. CHSB foam exhibited salt tolerance and high-salinity-enhanced foam stability, superior to the traditional foam (e.g., AOS) shown in Figs. S1-S2 (Supplementary Materials). Surprisingly, the foam half-life continuously decreased as the CHSB concentration increased from 0.05 to 1.00 wt%.

It is well documented that drainage occurs immediately after foam generation and causes $f_{\rm w}$ to decline rapidly. Subsequently, coarsening and coalescence govern foam stability and $f_{\rm w}$ (Fameau

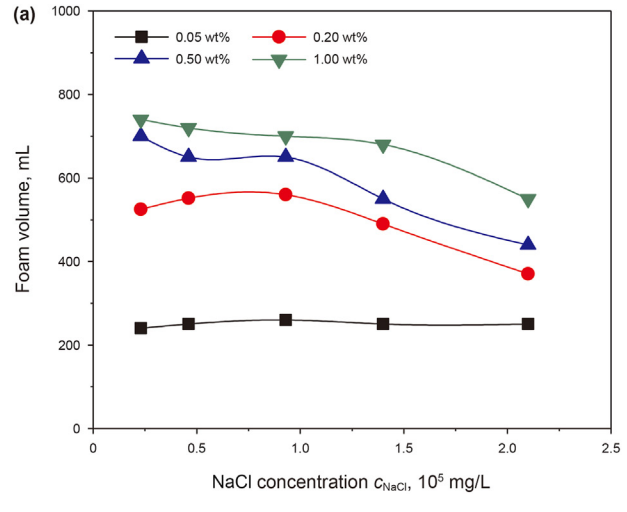
and Salonen, 2014). If the coalescence is weak, f_w will level off in a long time, and coarsening dominates the foam decay; otherwise, $f_{\rm w}$ increases continuously. Therefore, we plotted $f_{\rm w}$ against time at different salinities to further analyze the influence of salinity on foam decay. Fig. 8 shows that, with increasing salinity, the slopes of the $f_{\rm w}$ curves in the early period of foam decay are similar, but the plateaus of the curves are extended. Meanwhile, the values of f_w corresponding to the turning points of the f_w curves increase with salinity, that is, the higher the salinity, the thicker the foam film and the slower the coarsening. These findings indicate that high salinity can enhance foam stability by hampering coarsening and coalescence. The coarsening and coalescence closely depend on the dilatational viscoelasticity and thin-film thickness (Biance et al., 2011; Zhang and Sharma, 2015). Therefore, the effects of salinity on surface behaviors and thin-film drainage of CHSB were subsequently investigated.

3.2. Influence of salinity on surface behavior

3.2.1. Dilatational viscoelasticity

The measurements of dilatational viscoelasticity were conducted at different salinities and CHSB concentrations. The results of 0.20 wt% CHSB are presented in Figs. 9 and 10, and those of other CHSB concentrations are shown in Figs. S4 and S5 (Supplementary Materials).

Fig. 9 shows that the dilatational modulus decreases with CHSB concentration and increases with salinity. Comparing Fig. 9 with Fig. 7 shows that the response of dilatational modulus to salinity was in line with that of foam stability. According to Eq. (2), the dilatational modulus is inversely proportional to the deformation degree of the surface area, which can reflect the capability of a surface to resist deformation. The film with a higher dilatational modulus deformed less at a given stress, thereby being less likely to rupture. Meanwhile, the film with a high dilatational modulus tends to maintain thickness, which leads to low film permeability and slow coarsening (Tcholakova et al., 2011, 2017; Pagureva et al., 2016). Fig. 10 demonstrates that the surface formed by CHSB molecules presents viscoelastic features within the frequency range of 0.02-2 Hz. The dilatational elasticity and viscidity of the CHSB surface were both enhanced with salinity. However, the increase of the elastic modulus was more evident than that of the viscous modulus at all the tested CHSB concentrations, indicating that the positive response of dilatational modulus to salinity was chiefly



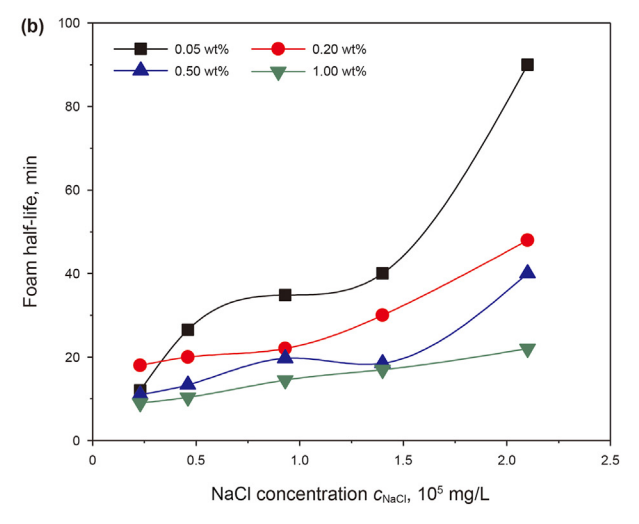


Fig. 7. (a) Foam volume and (b) foam half-life as a function of NaCl concentration at different CHSB concentrations (from 0.05 wt% to 1.00 wt%).

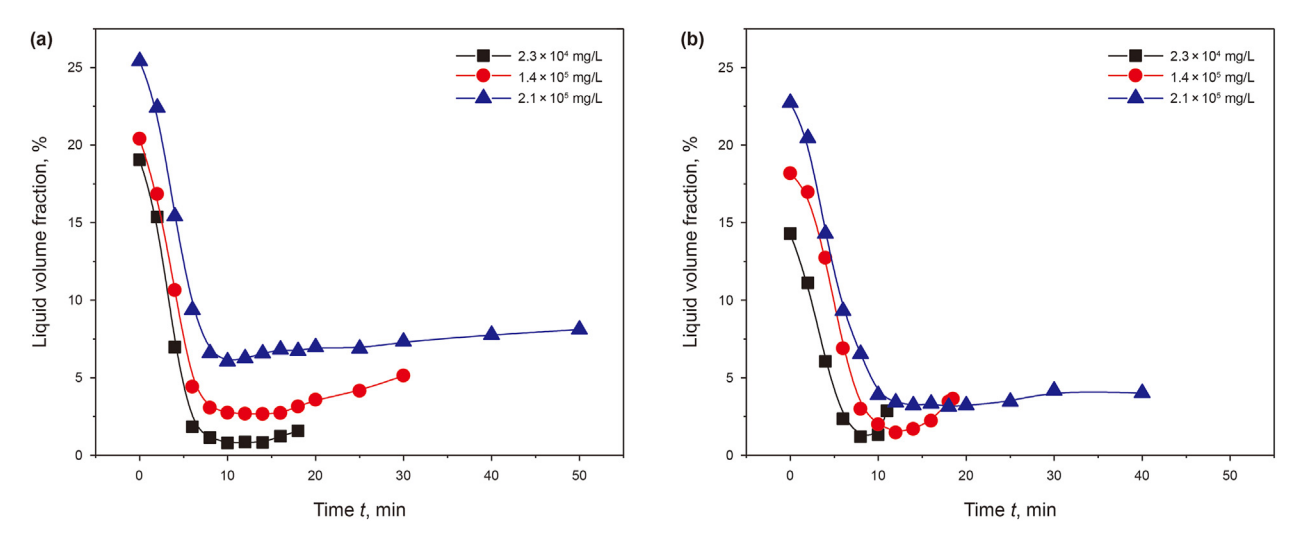


Fig. 8. Liquid volume fraction over time within foam half-life at varied salinities. The foams were generated by (a) 0.20 wt% CHSB and (b) 0.50 wt% CHSB solution, respectively.

12

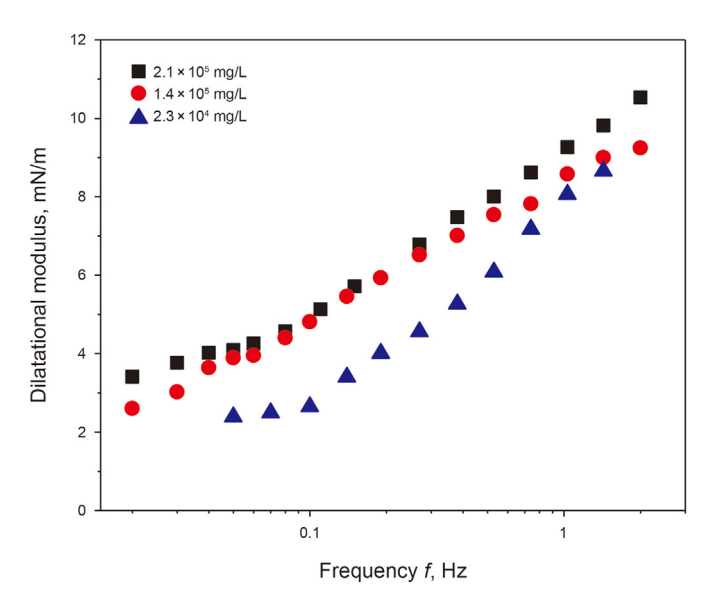
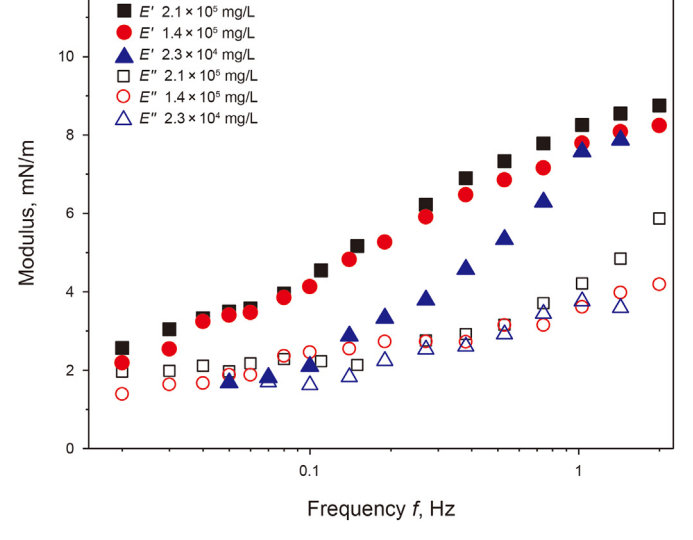


Fig. 9. Effect of NaCl concentration on the dilatational modulus. The CHSB concentration was $0.20~\rm wt\%$.



 $\begin{tabular}{ll} \textbf{Fig. 10.} & \textbf{Effect of NaCl concentration on elastic and viscous moduli.} & \textbf{The CHSB concentration was 0.20 wt\%.} \end{tabular}$

contributed by elasticity. It has long been recognized that dilatational elasticity plays a crucial role in foam stability (Wang et al., 2016). Therefore, the high dilatational modulus and surface elasticity induced by high salinity were critical to the superior stability of CHSB foam.

The strength of surface elasticity was determined by the intensity of lateral interaction among surfactant molecules on the surface (Lucassen and Tempel, 1972; Wang et al., 2019). High salinity improved the elastic moduli, suggesting that the intermolecular interaction on the surface strengthened with increasing salinity. This interaction is related to the number of surfactant molecules on the surface and the interaction between each pair of surfactant molecules. Therefore, we evaluated the absorption behavior of the CHSB molecules on the gas—liquid surface, as described in the next section.

3.2.2. Absorption behavior

3.2.2.1. Maximum surface excess concentration. The surface tensions of solutions with different CHSB concentrations were

measured at salinities of 2.3×10^4 and 2.1×10^5 mg/L. The surface tension — CHSB concentration curves are presented in Fig. 11, and the adsorption parameters calculated based on Eqs. (4) and (5) are summarized in Table 1.

Table 1 shows that Γ_{max} increases and A_{min} decreases with increasing salinity, indicating that the CHSB molecules packed more densely at higher salinity. Based on the chemical structure of CHSB (Fig. 3), the hydrophilic group of CHSB contains both a negative ion (SO $_3^2$) and a positive ion (N $^+$). Although the CHSB solution was electrically neutral at pH = 7, electrostatic repulsion exists between the same charged head group. In CHSB brine solution, attraction exists between counterions (i.e., between Na $^+$ and SO $_3^2$ and between Cl $^-$ and N $^+$) while repulsion exits between homoions (i.e., between Na $^+$ and N $^+$ and between Cl $^-$ and SO $_3^2$), so the impact of salt on CHSB was weaker than that on anionic surfactants. The electrostatic repulsion was screened owing to the attraction between counter-ions, which promoted the adsorption of CHSB molecules. More molecules accumulated on the surface would yield a higher surface tension gradient during surface

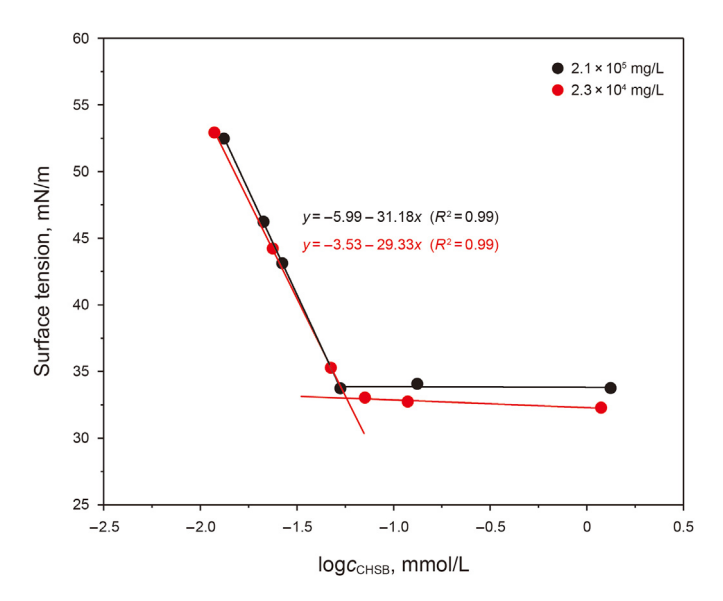


Fig. 11. Surface tension as a function of CHSB concentration at NaCl concentrations of 2.3×10^4 and 2.1×10^5 mg/L.

 $\ln(\gamma_t - \gamma_{eq}) = \ln(\gamma_0 - \gamma_{eq}) - kt$ (11)

where γ_t is the surface tension of the surfactant solution at a given time t; and γ_0 is the surface tension of the solvent. We measured the dynamic surface tension of CHSB solutions with varied salinities and CHSB concentrations and plotted the curves of $\ln(\gamma_t - \gamma_{\rm eq})$ versus t, as presented in Fig. 12.

Fig. 12 illustrates that the curves fall into two distinct regions. In region I, the surface tension dropped promptly, and the surface adsorption of CHSB molecules was controlled by diffusion (Eastoe and Dalton, 2000). In region II, the surface tension gradually reached an equilibrium state, and the surface adsorption had to overcome an adsorption barrier. Therefore, the value of *k* was equal to the slope of the curve in region I. As listed in Table 2, *k* decreases with salinity, indicating that the addition of salt decelerated the diffusion of CHSB molecules. Hence, the surface tension gradient caused by surface deformation could not be timely eliminated by the CHSB molecules of the bulk phase. This facilitated the transportation of the CHSB molecules and accompanying liquid molecules on the surface, leading to high dilatational viscoelasticity.

 Table 1

 Equilibrium adsorption parameters of CHSB solution.

NaCl concentration, mg/L	CMC, wt%	$\gamma_{ m cmc,}$ mN/m	$\Gamma_{ m max}$, $10^{-10}~{ m mol/cm^2}$	A_{\min} , nm ²
$\begin{array}{c} 2.3 \times 10^4 \\ 2.1 \times 10^5 \end{array}$	0.0018	33.02	5.228	0.318
	0.0017	33.86	5.558	0.299

deformation, causing the increased dilatational modulus. Additionally, both hydrogen bonding and hydrophobic association intensified with $\Gamma_{\rm max}$, which increased the interaction between CHSB molecules on the surface and thus increased the elastic modulus (Huang et al., 2007). According to Table 1, the CHSB concentrations used in this study were all above the CMC, implying that the amount of CHSB molecules on the gas—liquid surface was constant. In other words, the interaction between CHSB molecules on the surface should be insensitive to the CHSB concentration. However, Figs. 9 and 10 and Figs. S4—S5 (Supplementary Materials) show that the dilatational and elastic moduli both decreases with CHSB concentration. Hence, other factors besides $\Gamma_{\rm max}$ affected the dilatational viscoelasticity.

As shown in Fig. 10, the elasticity modulus increases with oscillation frequency. It is widely accepted that the increase in oscillation frequency accelerates the surface deformation, which gives surfactant molecules in the bulk phase insufficient time to absorb on the newly formed surface (Cui et al., 2011; Pu et al., 2018). Thus, as oscillation frequency increases, more CHSB molecules from the adjacent surface with the accompanying liquid molecules migrate to the deformed surface to repair the film thickness, which enhances the Marangoni effect and increases the elasticity modulus. Accordingly, it is reasonable to speculate that the variation of dilatational viscoelasticity induced by salinity and CHSB concentration might also relate to the diffusion dynamics of CHSB molecules.

3.2.2.2. Diffusion rate. The decrease in surface tension originates from the adsorption of surfactant molecules at the gas—liquid surface. Hence, the reduction velocity of surface tension (k) defined in the following equation can be used to evaluate the diffusion rate of surfactant molecules (Gong et al., 2020):

Table 2 also shows that k increases by a factor of 17 when CHSB concentration increases from 0.05 to 0.50 wt%, which supports the finding that k was negatively correlated with the dilatational viscoelasticity.

3.3. Dynamics of thin-film drainage

The amount of liquid that drains out of the thin film is insignificant compared with the initial drainage. However, the thin-film drainage will alter the film thickness and thus significantly impact the coarsening and coalescence. Given that the response of foam stability to salinity was independent of the CHSB concentration, we chose 0.20 wt% CHSB to quantitatively and visually investigate the effect of salinity on the dynamics of thin-film drainage.

3.3.1. Interferograms of thin film

As shown in Fig. 13, blue and orange regions appear in the interferograms at the early stage of thin-film drainage. According to the interference color chart in Fig. 6, the brilliant colors indicate that the film thickness is > 100 nm. The colorful regions faded and radially expanding gray domains presented as the film thickness decreased to < 100 nm. The CHSB micelles self-organized into a layered structure in the confined thin film during drainage. The chemical potential gradient triggered a layer of micelles to diffuse toward the meniscus (Kralchevski et al., 1990; Lee et al., 2016), leading to vacancies and the subsequent dark spots in the parallel film (Fig. 14). The osmotic pressure of the dark spot was lower than that of its periphery because of the decreased micelle concentration (Kralchevski et al., 1990; Nikolov and Wasan, 2022), causing the outflowing of liquid and the formation of thinner gray domains with a metastable thickness. Subsequently, the micelles were driven out layer by layer until no micelles were left in the film, and the film correspondingly thinned stepwise until a common black

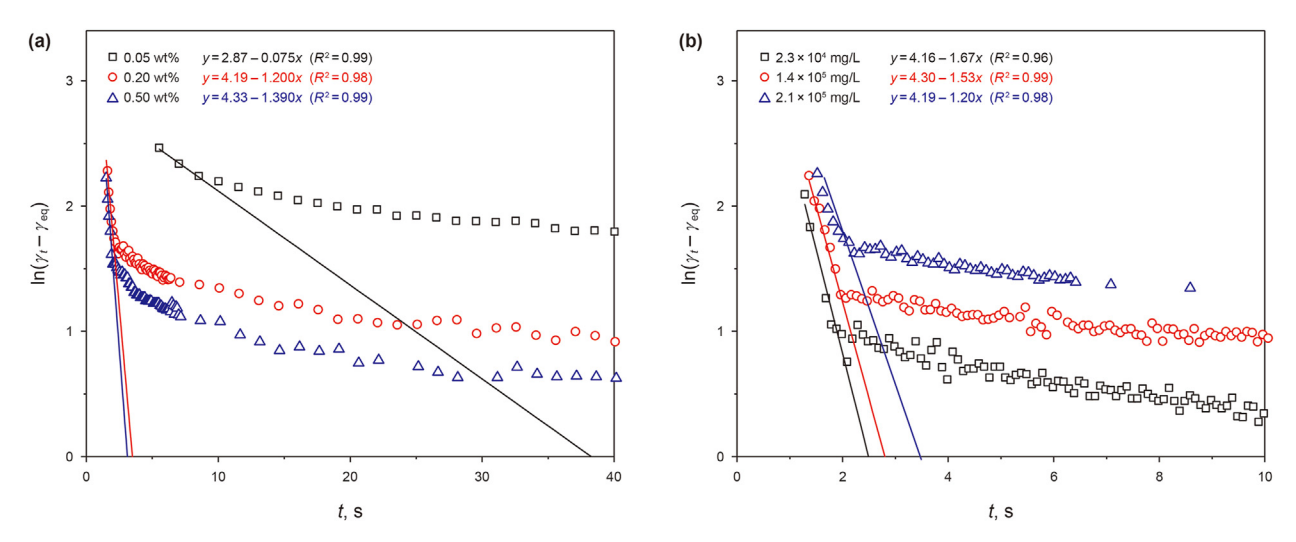


Fig. 12. $\ln(\gamma_t - \gamma_{eq})$ as a function of time for CHSB solutions with different (a) CHSB concentrations and (b) NaCl concentrations.

Table 2Reduction velocities of surface tension at different concentrations of NaCl and CHSB.

NaCl concentration, mg/L	CHSB concentration, wt%	k	R^2
2.3×10^4	0.20	1.67	0.96
1.4×10^{5}	0.20	1.53	0.99
2.1×10^5	0.20	1.20	0.98
2.1×10^{5}	0.05	0.075	0.99
2.1×10^{5}	0.50	1.39	0.99

film formed. The thin film became progressively less reflective because of the reduced thickness, resulting in the darkening interferogram. White spots were found assembled surrounding the growing black domains (e.g., the red circle in Fig. 13), and the reconstructed film-thickness map (Fig. 14) revealed that their thickness was greater than that in the other areas. Yilixiati et al. (2018) also observed white spots generated during the thin-film drainage in the presence of salt and proposed that these white

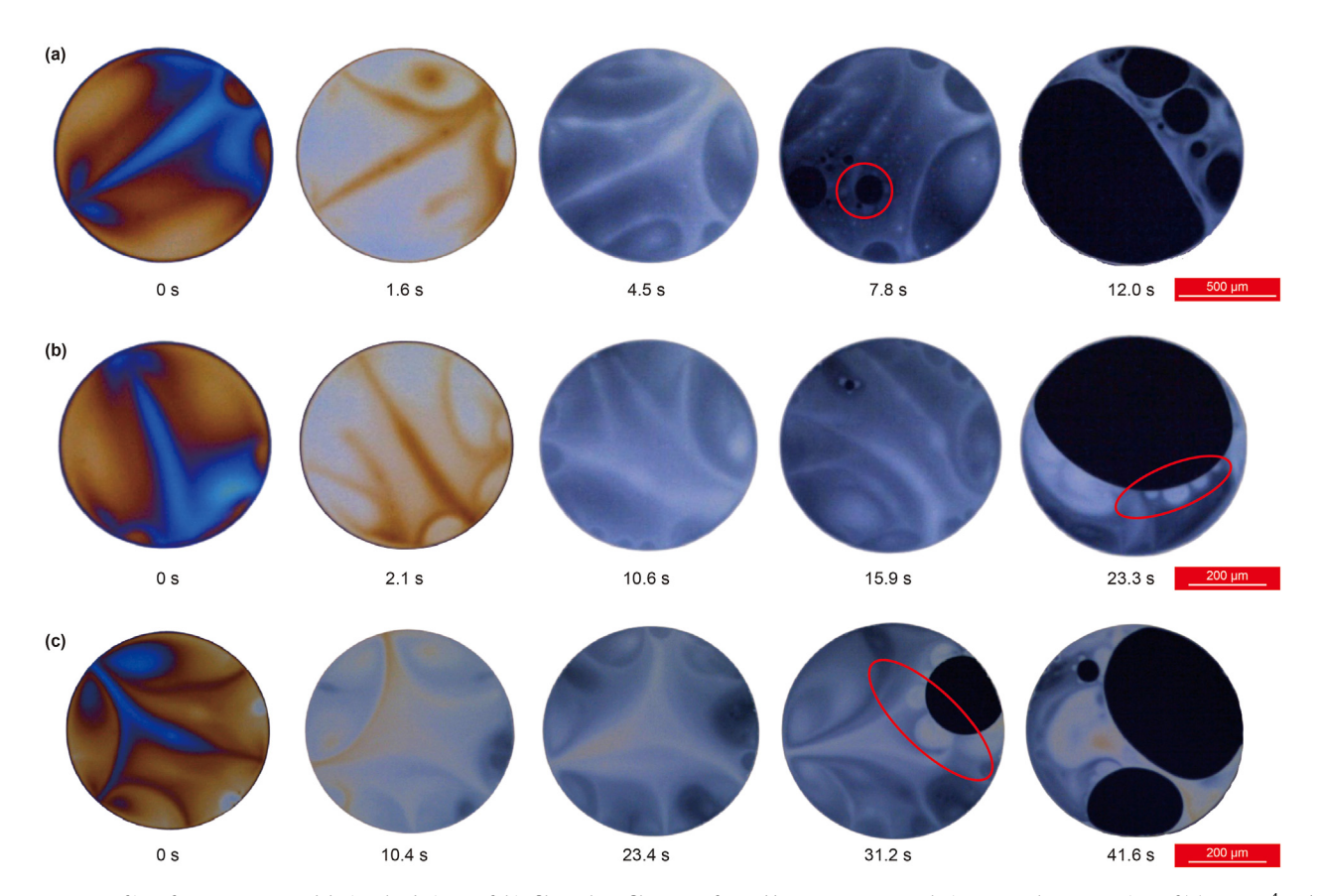


Fig. 13. Sequence of interferograms captured during the drainage of thin films. These films were formed by 0.20 wt% CHSB solutions at NaCl concentrations of (a) 2.3×10^4 mg/L, (b) 1.4×10^5 mg/L, and (c) 2.1×10^5 mg/L, respectively. As the salinity increased, the drainage decelerated, and the white spots enlarged.

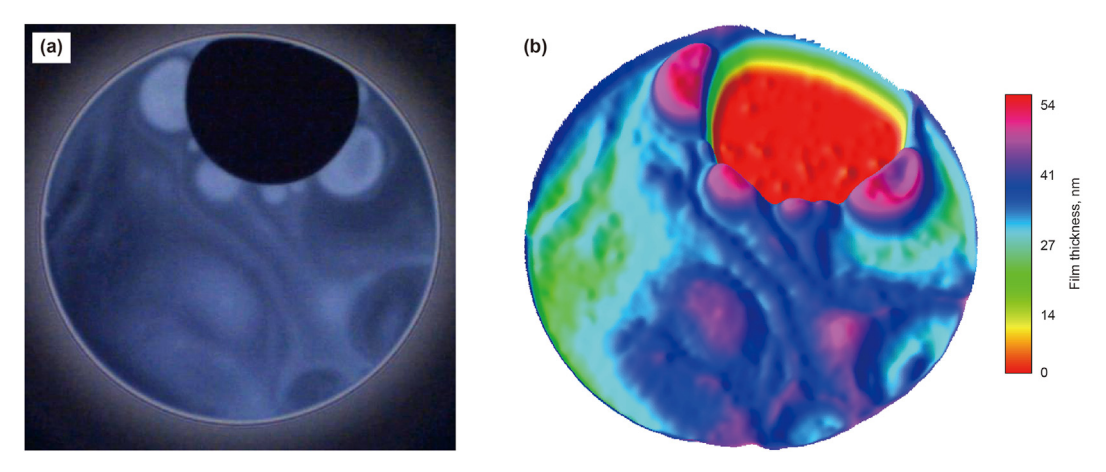


Fig. 14. (a) Typical interferogram during thin-film drainage at 1.4×10^5 mg/L NaCl (t = 19.5 s) and (b) its 3D thickness map.

spots consisted of micelles and liquid that failed to reach the meniscus in time.

Fig. 13 shows that the darkening of the CHSB thin film was decelerated with increasing salinity, suggesting that high salinity mitigated the thin-film drainage and stabilized the film. The drainage rate of the CHSB thin film was much slower than that of the traditional surfactant thin film at the same salinity (Fig. S3 (Supplementary Materials)), which was consistent with its superior foam stability. To characterize the effect of salinity on the process of stepwise thinning, we analyzed the variation and transition of film thickness, as described in the next subsection.

3.3.2. Temporal evolution of thin-film thickness

We estimated the film thickness evolution at various salinities using the colorimetric method, and the results are presented in Fig. 15 and Table 3.

As shown in Fig. 15, the film thickness curves exhibit four horizontal platforms, indicating that the drainage of thin films experienced four metastable film thicknesses. With the increase in salinity, the step number of film thinning remained constant, while the average step size (Δh) decreased (Table 3). Based on the previous finding in the absorption behavior, the electrostatic repulsion between CHSB molecules weakened with salinity; likewise, the

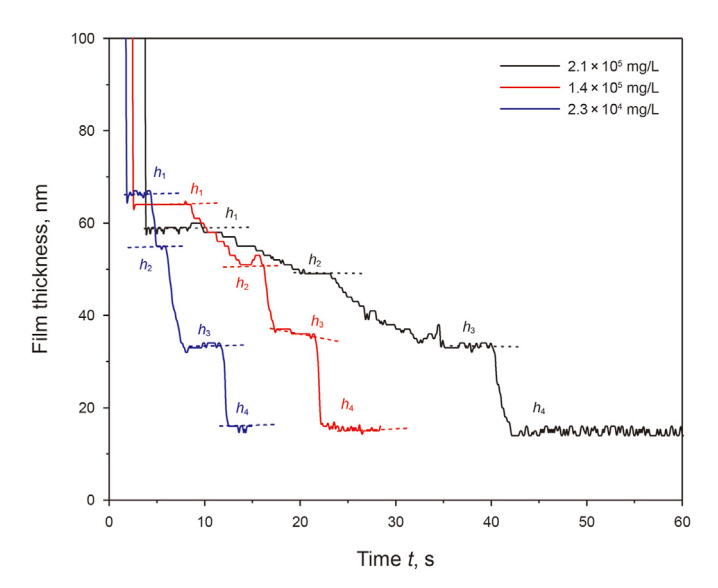


Fig. 15. Evolution of film thickness over time at different NaCl concentrations.

Table 3Parameters for characterizing the stepwise thinning.

NaCl concentration, mg/L	Δh , nm	Δt, s	Δ <i>t</i> , s		
		Δt_1	Δt_2	Δt_3	
2.3 × 10 ⁴	17.0	2.9	3.5	4.2	
1.4×10^{5}	16.3	11.0	5.3	5.0	
2.1×10^{5}	14.7	16.6	14.6	7.0	

intermicellar interaction was also reduced at elevated salinity. Consequently, a denser micellar layered structure with a shorter intermicellar distance was formed as salinity increased. In much of literature it has been argued that Δh was approximately equal to the distance between each layer of micelles (Dimitrova et al., 2004; Abbott, 2004; Lee et al., 2017; Ochoa et al., 2021). Therefore, Δh decreased with salinity because of the compacted micellar structure. Kemal et al. (2021) and Tabor et al. (2011) observed a similar decrease in Δh with salinity using light scattering, atomic force microscopy, and neutron scattering data.

The transition time from one metastable state to the next was termed the step time (Δt). Table 3 indicates that Δt increased with salinity. Prior research has demonstrated that the transition of film thickness requires a jump over the energy barrier, that is, the peak of the disjoining pressure curves. For instance, the transition from metastable thickness $h_{\rm c}$ to $h_{\rm d}$ needs to get over the energy barrier $\Pi_{\rm cd}$ (Fig. 2) (Yilixiati et al., 2018). For a micellar solution, the energy barrier was mainly contributed by $\Pi_{\rm OS}$ (Zeng et al., 2011), which can be estimated by the following model (Zhang and Sharma, 2018; Yilixiati et al., 2018):

$$\Pi_{\text{OS}} = \frac{(c - \text{CMC})N_{\text{A}}}{N_{\text{agg}}} f(\varphi) K_{\text{B}} T \cos\left(\frac{2\pi h}{\Delta h}\right) \exp\left[\left(\left(\frac{d}{\Delta h}\right)^{3} - \frac{h}{\Delta h}\right) g(\varphi)\right]$$
(12)

$$f(\varphi) = \frac{(1 + \varphi + \varphi^2 - \varphi^3)}{(1 - \varphi)^3}$$
 (13)

$$g(\varphi) = \frac{\sqrt{2/3} + a_1 \Delta \varphi + a_2 (\Delta \varphi)^2}{(b_1/\Delta \varphi) - b_2}$$
 (14)

where $N_{\rm agg}$ is the aggregation number of micelles; d is the micelle size; φ is the effective volume fraction of the micelles, defined as

 $\varphi=6\pi d^3/6; f(\varphi)$ is the compressibility factor; $g(\varphi)$ is the geometric factor; and a_1, a_2, b_1 , and b_2 are constants. Here, $\rho=\frac{(c-CMC)N_A}{N_{\rm agg}}$ was defined as the number density of micelles in a thin film, and $f(\varphi)$ was a positive function of $\rho\left(\varphi=6\pi d^3/6\right)$. The amplitude of $\Pi_{\rm OS}$ equaled $\rho f(\varphi)K_{\rm B}T$ and was positively correlated with ρ . It determined the energy barrier and thus the value of Δt .

Previous research has indicated that Δh was highly dependent on ρ . Anachkov et al. (2012) probed the stepwise thinning process of six surfactant solutions through experimental datasets and theoretical approaches, corroborating that Δh varied with a power law of $\Delta h \propto \rho^{-1/3}$. Zeng et al. (2015) experimentally observed the thin-film stability of silica nanoparticle suspensions using smallangle X-ray scattering and also found that Δh is equal to $\rho^{-1/3}$. Considering the decreased Δh with salinity, we inferred that ρ increased at elevated salinity. Therefore, the amplitude of Π_{OS} increased with increased salinity, and the film would take longer to reach the following metastable film thickness at higher salinity. The tighter compaction of CHSB micelles in the thin film hindered the diffusion of micelles, and the enlarged white spots induced by high salinity (Fig. 13) provided direct evidence for this. In summary, high salinity increased the energy barrier of film thinning and inhibited micelle diffusion, thereby decelerating the drainage of the thin film.

3.4. Limitations

The measurements of surface behavior and the dynamic drainage of thin film proceeded at room temperature (or $20\,^{\circ}\text{C}$) and atmospheric pressure due to the lack of corresponding testing techniques in high-temperature environments. The foam decay process and surface behavior of surfactant will influence by temperature and pressure. Therefore, more comprehensive work is needed to understand the high-salinity-enhanced stability of CHSB foam in reservoir environments.

4. Conclusions

In this study, we examined the decay processes of CHSB foams under a wide range of CHSB and NaCl concentrations. The results showed that the initial drainage of CHSB foam was insensitive to salinity, whereas coarsening and coalescence were inhibited by elevated salinity. As NaCl concentration increased from 2.3×10^4 to 2.1×10^5 mg/L, the foam half-life could be prolonged by a factor of 6.5. The surface behavior and thin-film spatiotemporal evolution were characterized to understand the stability of the high-salinity enhanced foam. With increasing salinity, the number of CHSB molecules absorbing on the gas-liquid surface increased, and the diffusion rate decreased, resulting in the increased dilatational modulus and surface elasticity. The increase in dilatational viscoelasticity decelerated the coarsening and coalescence, thus dominating the high-salinity-enhanced foam stability. The CHSB film with a thickness of ~100 nm underwent four stepwise thinning processes to become a common black film. The increased ρ and Π_{OS} at elevated salinity caused the step size to decrease and the film thickness transition to slow, which weakened the thin-film drainage and thus the coarsening and coalescence.

Declaration of competing interest

The authors declare the following financial interests/personal relationships which may be considered as potential competing interests: Lin Sun reports financial support was provided by National Natural Science Foundation of China (No. 51904256).

Acknowledgements

The authors would like to be grateful for the financial support of National Natural Science Foundation of China (No. 51904256). And special thanks to the valuable comments made by the anonymous reviewers.

Appendix A. Supplementary data

Supplementary data to this article can be found online at https://doi.org/10.1016/j.petsci.2023.01.012.

References

- Abbott, A.P., 2004. Application of hole theory to the viscosity of ionic and molecular liquids. ChemPhysChem 5 (8), 1242–1246. https://doi.org/10.1002/cphc.200400190.
- Agra, P.R., Tayfun, B., 2022. A review of the mechanics of heavy-oil recovery by steam injection with chemical additives. J. Petrol. Sci. Eng. 208 (Part D). https:// doi.org/10.1016/j.petrol.2021.109717.
- Alzobaidi, S., Da, C., Tran, V., et al., 2017. High temperature ultralow water content carbon dioxide-in-water foam stabilized with viscoelastic zwitterionic surfactants. J. Colloid Interface Sci. 488, 79–91. https://doi.org/10.1016/ j.jcis.2016.10.054.
- Amani, P.A., Miller, R.B., Ata, S.C., et al., 2020. Dynamics of interfacial layers for sodium dodecylbenzene sulfonate solutions at different salinities. J. Ind. Eng. Chem. 92, 174–183. https://doi.org/10.1016/j.jiec.2020.09.002.
- Anachkov, S.E., Danov, K.D., Basheva, E.S., et al., 2012. Determination of the aggregation number and charge of ionic surfactant micelles from the stepwise thinning of foam films. Adv. Colloid Interface Sci. 183, 55–67. https://doi.org/10.1016/j.cis.2012.08.003.
- Babamahmoudi, S., Riahi, S., 2018. Application of nano particle for enhancement of foam stability in the presence of crude oil. J. Mol. Liq. 264, 499–509. https://doi.org/10.1016/j.molliq.2018.04.093.
- Biance, A.L., Delbos, A., Pitois, O., 2011. How topological rearrangements and liquid fraction control liquid foam stability. Phys. Rev. Lett. 106 (6), 68301. https:// doi.org/10.1103/PhysRevLett.106.068301.
- Cui, X.H., Zhang, L., Zhao, R.-H., et al., 2011. Interfacial interactions among aromatic side chained N-acyltaurates studied by interfacial tension relaxation measurements. Chem. J. Chin. Univ. 32 (7), 1556–1562 (in Chinese).
- Da, C., Alzobaidi, S., Jian, G., et al., 2018. Carbon dioxide/water foams stabilized with a zwitterionic surfactant at temperatures up to 150 °C in high salinity brine. J. Petrol. Sci. Eng. 166, 880–890. https://doi.org/10.1016/j.petrol.2018.03.071.
- Dimitrova, T.D., Leal-Calderon, F., Gurkov, T.D., et al., 2004. Surface forces in model oil-in-water emulsions stabilized by proteins. Adv. Colloid Interface Sci. 108–109, 73–86. https://doi.org/10.1016/j.cis.2003.10.003.
- Eastoe, J., Dalton, J.S., 2000. Dynamic surface tension and adsorption mechanisms of surfactants at the air-water interface. Adv. Colloid Interface Sci. 85 (2–3), 103–144. https://doi.org/10.1016/s0001-8686(99)00017-2.
- Eiki, G., Murat, D., Takashi, K., et al., 2003. Computer-synthesis of an interference color chart of human tear lipid layer, by a colorimetric approach. Invest. Ophthalmol. Vis. Sci. 44 (11), 4693–4697. https://doi.org/10.1167/iovs.03-0260.
- Fameau, A.L., Salonen, A., 2014. Effect of particles and aggregated structures on the foam stability and aging. Cr. Phys. 15 (8–9), 748–760. https://doi.org/10.1016/ i.crhv.2014.09.009.
- Ghosh, P., Mohanty, K.K., 2019. Study of surfactant alternating gas injection (SAG) in gas-flooded oil-wet, low permeability carbonate rocks. Fuel 251, 260–275. https://doi.org/10.1016/j.fuel.2019.03.119.
- Gong, Z.M., Wang, R.X., Xie, M.B., 2020. Investigation on adsorption characteristics of perfluoroalkyl surfactants. CIE J. 71 (4), 1754–1761. https://doi.org/10.11949/ 0438-1157.20190868 (in Chinese).
- Hongyan, C., Jian, F., Dong, H., et al., 2017. Development of large-hydrophobe betaine surfactants for chemical enhanced oil recovery in low/high salinity reservoirs. In: SPE Kingdom of Saudi Arabia Annual Technical Symposium and Exhibition. https://doi.org/10.2118/188053-MS.
- Hu, L.Z., Sun, L., Zhao, J.Z., et al., 2020. Influence of formation heterogeneity on foam flooding performance using 2D and 3D models: an experimental study. Petrol. Sci. 17 (3), 734–748. https://doi.org/10.1007/s12182-019-00408-x.
- Huang, Y., Zhang, L., Zhang, L., et al., 2007. Dynamic interfacial dilational properties of hydroxy-substituted alkyl benzenesulfonates. J. Phys. Chem. B 111 (20), 5640–5647, 5647.10.1021/jp070997t.
- Kang, W., Jiang, H., Yang, H., et al., 2021. Study of nano-SiO₂ reinforced CO₂ foam for anti-gas channeling with a high temperature and high salinity reservoir. J. Ind. Eng. Chem. 97, 506–514. https://doi.org/10.1016/j.jiec.2021.03.007.
 Kedir, A.S., Solbakken, J.S., Aarra, M.G., 2022. Foamability and stability of anionic
- Kedir, A.S., Solbakken, J.S., Aarra, M.G., 2022. Foamability and stability of anionic surfactant-anionic polymer solutions: influence of ionic strength, polymer concentration, and molecular weight. Colloids Surf., A 632, 127801. https:// doi.org/10.1016/i.colsurfa.2021.127801.
- Kemal, S.I., Ortiz, C.A.U., Sharma, V., 2021. Surface forces and stratification in foam films formed with bile salts. Mol. Syst. Des. Eng. 6 (7), 520–533. https://doi.org/

10.1039/d0me00024h.

- Keshavarzi, B., Mahmoudvand, M., Javadi, A., et al., 2020. Salt effects on formation and stability of colloidal gas aphrons produced by anionic and zwitterionic surfactants in xanthan gum solution. Colloids and Interf. 4 (1), 9. https:// doi.org/10.3390/colloids4010009.
- Khan, A., Saxena, S., Baloni, S., et al., 2021. Overview and methods in enhanced oil recovery. J. Phys. Conf. Ser. 2070, 012061. https://doi.org/10.1088/1742-6596/ 2070/1/012061.
- Kralchevski, P., Nikolov, A., Wasan, D.T., et al., 1990. Formation and expansion of dark spots in stratifying foam films. Langmuir 6 (6), 1180–1189. https://doi.org/10.1021/la00096a026.
- Langevin, D., 2020. On the rupture of thin films made from aqueous surfactant solutions. Adv. Colloid Interface Sci. 275, 102075. https://doi.org/10.1016/ i.cis.2019.102075.
- Lee, J., Nikolov, A., Wasan, D., 2017. Stepwise thinning dynamics of a foam film formed from an anionic micellar solution. J. Petrol. Sci. Eng. 487, 217–222. https://doi.org/10.1016/j.jcis.2016.10.048.
- Lee, J., Nikolov, A., Wasan, D., 2016. Stratification of a foam film formed from a nonionic micellar solution: experiments and modeling. Langmuir 32 (19), 4837–4847. https://doi.org/10.1021/acs.langmuir.6b00561.
- Li, S., Wang, Q., Li, Z., 2020. Stability and flow properties of oil-based foam generated by CO₂. SPE J. 25 (1), 416–431. https://doi.org/10.2118/199339-PA.
- Li, W., Wei, F., Xiong, C., et al., 2019. Effect of salinities on supercritical CO₂ foam stabilized by betaine surfactant for improving oil recovery. Energy Fuel. 33 (9), 8312–8322. https://doi.org/10.1021/acs.energyfuels.9b01688.
- 8312–8322. https://doi.org/10.1021/acs.energyfuels.9b01688. Liu, Q., Zhang, Y., Zhao, X., et al., 2022. Enhanced oil recovery by foam flooding using foam stabilized with modified Fe_3O_4 nanoparticles. J. Petrol. Sci. Eng. 209, 109850. https://doi.org/10.1016/j.petrol.2021.109850.
- Liu, Z.D., Bian, J., Wang, J., et al., 2010. Computer simulation and application of white light interference color. Chin. J. Lasers 37 (S1), 303–307. https://doi.org/ 10.3788/CJL201037s1. 0303 (in Chinese).
- Liu, Z.M., Ge, J.J., Shi, X.J., et al., 2022. Development and performance evaluation of foaming agent for air flooding in reservoirs with high temperature and salinity. Special Oil Gas Reservoirs 29 (3), 118–123 (in Chinese).
- Lucassen, J., Tempel, M.V.D., 1972. Dynamic measurements of dilational properties of a liquid interface. Chem. Eng. Sci. 27 (6), 1283–1291. https://doi.org/10.1016/ 0009-2509(72)80104-0.
- Nikolov, A.D., Wasan, D.T., 2022. The foam film's stepwise thinning phenomenon and role of oscillatory forces. Adv. Colloid Interface Sci. 303, 102636. https://doi.org/10.1016/j.cjs.2022.102636.
- Ninham, B.W., Pashley, R.M., Nostro, P.L., 2017. Surface forces: changing concepts and complexity with dissolved gas, bubbles, salt and heat. Curr. Opin. Colloid Interface Sci. 27, 25–32. https://doi.org/10.1016/j.cocis.2016.09.003.
- Niu, R., Wang, C., Sun, Z., et al., 2017. A novel alkyl sulphobetaine gemini surfactant based on S-triazine: synthesis and properties. J. Surfactants Deterg. 20 (6), 1255–1262. https://doi.org/10.1007/s11743-017-1996-y.
- Ochoa, C., Gao, S., Srivastava, S., et al., 2021. Foam film stratification studies probe intermicellar interactions. P. Natl. Acad. Sci. USA 118 (25), e2024805118. https://doi.org/10.1073/pnas.2024805118.
- Pagureva, N., Tcholakova, S., Golemanov, K., et al., 2016. Surface properties of adsorption layers formed from triterpenoid and steroid saponins. Colloids Surf., A 491, 18–28. https://doi.org/10.1016/j.colsurfa.2015.12.001.
- Pu, W.F., Shen, C., Tang, X.J., et al., 2018. Research advances about oil-water interfacial dilational viscoelasticity in chemical flooding. Oilfield Chem. 35 (3), 562–570. https://doi.org/10.19346/j.cnki.1000-4092.2018.03.033 (in Chinese).
- Radke, C.J., 2015. Film and membrane-model thermodynamics of free thin liquid films. J. Colloid Interface Sci. 449, 462–479. https://doi.org/10.1016/ j.jcis.2014.12.079.
- Roncoroni, M.A., Romero, P., Montes, J., et al., 2021. Enhancement of a foaming formulation with a zwitterionic surfactant for gas mobility control in harsh reservoir conditions. Petrol. Sci. 18 (5), 1409–1426. https://doi.org/10.1016/ i.petsci.2021.08.004.
- Said, M.S., Jaafar, M.Z., Omar, S., et al., 2022. Influence of whey protein isolate on CO₂ foams stability in three different types of crude oil. Case Stud. Chem. Environ.

- Eng. 5, 100191. https://doi.org/10.1016/j.cscee.2022.100191.
- Shi, Q., Qin, B., Xu, Y., et al., 2022. Experimental investigation of the drainage characteristic and stability mechanism of gel-stabilized foam used to extinguish coal fire. Fuel 313, 122685, https://doi.org/10.1016/j.fuel.2021.122685.
- Suja, V.C., Kar, A., Cates, W., et al., 2018. Evaporation-induced foam stabilization in lubricating oils. P. Natl. Acad. Sci. USA 115 (31), 7919—7924. https://doi.org/ 10.1073/pnas.1805645115.
- Sun, L., Bai, B., Wei, B., et al., 2019. Recent advances of surfactant-stabilized N₂/CO₂ foams in enhanced oil recovery. Fuel 241, 83–93. https://doi.org/10.1016/j.fuel.2018.12.016.
- Sun, L., Wei, P., Pu, W., et al., 2016. The oil recovery enhancement by nitrogen foam in high-temperature and high-salinity environments. J. Petrol. Sci. Eng. 147, 485–494. https://doi.org/10.1016/j.petrol.2016.09.023.
- Syed, A.H., Yekeen, N., Padmanabhan, E., et al., 2020. Characterization of lauryl betaine foam in the Hele-Shaw cell at high foam qualities (80%-98%). Petrol. Sci. 17 (6), 1634–1654. https://doi.org/10.1007/s12182-020-00470-w.
- Tabor, R., Lockie, H., Chan, D.C., et al., 2011. Structural forces in soft matter systems: unique flocculation pathways between deformable droplets. Soft Matter 7 (24), 11334–11344. https://doi.org/10.1039/c1sm06326j.
- Tang, W., Sheng, J.J., 2022. Huff-n-puff gas injection or gas flooding in tight oil reservoirs? J. Petrol. Sci. Eng. 208 (Part D). https://doi.org/10.1016/ j.petrol.2021.109725.
- Tcholakova, S., Mitrinova, Z., Golemanov, K., et al., 2011. Control of Ostwald ripening by using surfactants with high surface modulus. Langmuir 27 (24), 14807–14819. https://doi.org/10.1021/la203952p.
- Tcholakova, S., Mustan, F., Pagureva, N., et al., 2017. Role of surface properties for the kinetics of bubble Ostwald ripening in saponin-stabilized foams. Colloids Surf., A 534, 16–25. https://doi.org/10.1016/j.colsurfa.2017.04.055.
- Varade, S.R., Ghosh, P., 2017. Foaming in aqueous solutions of zwitterionic surfactant: effects of oil and salts. J. Dispersion Sci. Technol. 38 (12), 1770–1784. https://doi.org/10.1080/01932691.2017.1283509.
- Wang, C., Fang, H., Gong, Q., et al., 2016. Roles of catanionic surfactant mixtures on the stability of foams in the presence of oil. Energy Fuel. 30 (8), 6355–6364. https://doi.org/10.1021/acs.energyfuels.6b01112.
- Wang, Z., Jin, Y., Wang, T., et al., 2019. Effect of branched chain and polyoxyethylene group on surface dilational rheology of cationic surfactants. Colloids Surf., A 577, 249–256. https://doi.org/10.1016/j.colsurfa.2019.05.063.
- Xie, Y., Li, J., Sun, T., et al., 2018. Synthesis, surface activity, and corrosion inhibition of dentritic quaternary ammonium salt-type tetrameric surfactants. J. Dispersion Sci. Technol. 39 (8), 1153–1159. https://doi.org/10.1080/ 01932691.2017.1385482.
- Xun, W., 2021. Application of chemical flooding in increasing yield of tertiary oil recovery. IOP Conf. Ser. Earth Environ. Sci. 781, 022066. https://doi.org/10.1088/ 1755-1315/781/2/022066.
- Yang, K., Li, S., Zhang, K., et al., 2021. Synergy of hydrophilic nanoparticle and nonionic surfactant on stabilization of carbon dioxide-in-brine foams at elevated temperatures and extreme salinities. Fuel 288, 119624. https://doi.org/ 10.1016/j.fuel.2020.119624.
- Yilixiati, S., Rafiq, R., Zhang, Y., et al., 2018. Influence of salt on supramolecular oscillatory structural forces and stratification in micellar freestanding films. ACS Nano 12 (2), 1050–1061. https://doi.org/10.1021/acsnano.7b05391.
- Zeng, Y., Grandner, S., Oliveira, C.P., et al., 2011. Effect of particle size and Debye length on order parameters of colloidal silica suspensions under confinement. Soft Matter 7 (22), 10899–10909. https://doi.org/10.1039/C1SM05971H.
- Zeng, Y., Schön, S., von Klitzing, R., 2015. Silica nanoparticle suspensions under confinement of thin liquid films. J. Colloid Interface Sci. 449, 522–529. https:// doi.org/10.1016/j.jcis.2015.02.019.
- Zhang, Y., Sharma, V., 2015. Domain expansion dynamics in stratifying foam films: experiments. Soft Matter 11 (22), 4408–4417. https://doi.org/10.1039/c5sm000663
- Zhang, Y., Sharma, V., 2018. Thickness-dependent phase transition drives nanoridge-to-mesa instability in micellar freestanding films. Langmuir 34 (26), 7922–7931. https://doi.org/10.1021/acs.langmuir.8b01010.